Scanning Hall-probe microscopy for site-specific observation of microstructure in superconducting wires and tapes for the clarification of their performance bottlenecks

Higashikawa, Kohei
Department of Electrical Engineering, Graduate School of Information Science and Electrical Engineering, Kyushu University

Inoue, Masayoshi
Department of Electrical Engineering, Faculty of Engineering, Fukuoka Institute of Technology

Ye, Shujun
Center for Innovative Integrated Electronic Systems, Tohoku University

Matsumoto, Akiyoshi
National Institute for Materials Science

他

出版情報：Superconductor Science and Technology. 33 (6), pp.064005-, 2020-05-07. IOP Publishing
バージョン：
権利関係：

Scanning Hall-probe microscopy for site-specific observation of microstructure in superconducting wires and tapes for the clarification of their performance bottlenecks

Kohei Higashikawa[1], Masayoshi Inoue[2], Shujun Ye[3], Akiyoshi Matsumoto[4], Hiroaki Kumakura[4], Ryuji Yoshida[5], Takeharu Kato[5], Takato Machi[6], Akira Ibi[6], Teruo Izumi[6], and Takanobu Kiss[1]

[1] Department of Electrical Engineering, Graduate School of Information Science and Electrical Engineering, Kyushu University, Fukuoka 819-0395, Japan
[2] Department of Electrical Engineering, Faculty of Engineering, Fukuoka Institute of Technology, Fukuoka 811-0295, Japan
[3] Center for Innovative Integrated Electronic Systems, Tohoku University, Sendai 980-8572, Japan
[4] National Institute for Materials Science, Tsukuba 305-0047, Japan
[5] Nanostructures Research Laboratory, Japan Fine Ceramics Center, Nagoya 456-8587, Japan
[6] Research Institute for Energy Conservation, Department of Energy and Environment, National Institute of Advanced Industrial Science and Technology, Tsukuba 305-8564, Japan

E-mail: kohei@super.ees.kyushu-u.ac.jp

Received 15 February 2020, Revised 13 March 2020, Revised 26 March 2020
Accepted for publication xxxxxx
Published xxxxxx

Abstract

This paper reports a diagnostic method for clarifying performance bottlenecks in superconducting wires and tapes for their further performance enhancements. In particular, our achievements by scanning Hall-probe microscopy (SHPM), which worked well for selecting positions for microstructure observation by SEM, TEM, and X-ray CT, are introduced. This hybrid microscopy offers the information of the direct relationship between the performance of a practical-scale superconducting wire or tape and its origin in micro-scale or nano-scale structure. As such examples, characterization results for an MgB_2 multi-filamentary wire, a commercially available long RE-123 coated conductor, and a striated multi-filamentary coated conductor are reported in this paper through reviewing our past studies.

Keywords: RE-123 coated conductor, MgB_2 wire, local critical current distribution, scanning Hall-probe microscopy (SHPM), microstructure observation

1. Introduction

Various kinds of superconducting wires and tapes have been developed in order to bring further breakthroughs to superconducting applications which have been supported by matured superconducting wires such as Nb-Ti, Nb_3Sn, etc. For example, RE-123 (RE: Y, Gd, Sm, Eu, etc.) coated conductors [1-7] have high in-field critical current density with strong

mechanical substrates; they have been expected to be used for high-field magnet applications [8-11]. Furthermore, they have also been expected to be used for power applications such as rotation machines for wind turbine, electric aircraft, etc. recently [12, 13]. Bi-2223 tape is known as the most established high-temperature superconducting (HTS) tape [14]; they have already contributed to significant achievements in power transmission cables [15, 16] and even in high-field magnet applications [17-19]. MgB_2 wires have been mainly expected to be substitutes for conventional superconducting wires for helium free operation [20-22]; they have also been proposed to be used together with liquid hydrogen [23-25]. Iron-based superconducting wires and tapes can keep their critical current densities high up to very high magnetic field [26], and a long tape has been developed recently [27].

However, each superconducting wire or tape has problems to be solved for practical use. For example, RE-123 coated conductors have an issue on spatial homogeneity in local critical current. This not only influences the yield ratio of the product, but also might be a reason why many magnets encounter local burnouts [28-31]. MgB_2 wires should have higher critical current density for wider use. Furthermore, not only wires and tapes themselves, but also some additional processes on them should be established for practical use: striation, splicing, cabling, etc [32-35]. Therefore, regardless of the kinds of superconducting wires and tapes, an effective diagnostic method is indispensable for clarifying their performance bottlenecks.

Generally, the performance of a superconducting wire or tape is evaluated as critical current (density) through a four-probe transport method. Then, the origin of the performance is discussed by microstructure observation through SEM, TEM, etc. However, it is difficult to clarify direct relationship between them because of the difference in spatial scale and resolution. For example, critical current (density) evaluated by the four-probe method is a kind of information averaged between voltage taps, e.g., centimeter order or more. On the other hand, microstructure observation is carried out for a limited field of view, e.g., submillimeter order or less. This means that a characterization method bridging such a scale gap is crucial for direct understanding of the relationship between the performance and the microstructure of a superconducting wire or tape.

As such a method, our past achievements based on scanning Hall-probe microscopy (SHPM) are summarized in this paper. The SHPM is a kind of a magnetic measurement; by scanning a Hall sensor on a magnetized sample, magnetic field distribution on the sample can be obtained. All of the Hall sensors used in this study were commercial ones fabricated with epitaxial GaAs films by Arepoc s.r.o.: HHP-VC with the active area of 50 x 50 μm^2 developed for operation at temperature range of 1.5-350 K in magnetic field up to 5 T; the sensitivity was higher than 50 mV/T, and the noise level in our measurements was at least lower than 10 $\mu T/Hz^{1/2}$. Then spatial distributions of local critical current (density) in superconducting wires and tapes were successfully characterized by the SHPM for selecting positions for microstructure observations. As a result, such site-specific observations worked very well for clarifying their performance bottlenecks.

2. Characterization of IMD Processed MgB_2 Multi-filamentary Wire

2.1. Sample and Experimental

The first example is characterization of an MgB_2 multi-filamentary wire. Figure 1 shows an illustration of the sample. The wire was fabricated by internal Mg diffusion (IMD) process known as a process bringing higher critical current density than that by the power-in-tube (PIT) process [36]. Mg atoms in rod diffused into surrounding B powder during annealing; then cylindrical MgB_2 with a hole was formed as a filament as shown in Figure 1(a). SiC was added to the B powder to enhance in-field properties. To characterize local critical current distribution in the filament by SHPM, the sample was polished as shown in Figure 1(b). An optical micrograph of the polished sample is shown in Figure 1(c). After cooling the sample below its critical temperature, external magnetic field, B_{ex}, was applied in z direction in order to magnetize the sample; then z component of magnetic field, B_z, was measured in the xy plane by an SHPM system [37, 38].

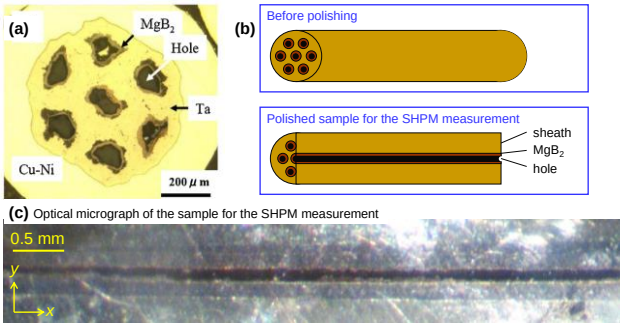

Figure 1. (a) optical micrograph of a cross-section of the MgB_2 multi-filamentary wire fabricated with IMD process [36], (b) illustration of the sample preparation for the SHPM measurement, and (c) optical micrograph of the polished plane for the SHPM measurement.

2.2. Local Critical Current Distribution in the Sample

Figure 2 shows the results obtained in a remanent state after the application of sufficiently high external magnetic field at 10 K. The magnetic field distribution shown in the lower part was taken with step size of 25 μm in x direction and 5 μm in y direction with contacting the sensor to the sample surface; it took 60 minutes to take the image. It can be seen that magnetic

field is trapped in each filament: not only in the central filament (Filament C) but also in the adjacent filaments (Filament U and Filament L). The local magnetic field intensity should be proportional to local critical current at a longitudinal position in each filament because the magnetization current should flow at the amplitude of critical current density. By plotting the magnetic field intensity immediately above a filament as a function of its longitudinal position, longitudinal distribution of local critical current in each filament, $I_{c,f}$, can be estimated as shown in the upper part of the figure; the value is normalized by its average for each filament, I_{c,f_ave}. Although the absolute value is not evaluated at this stage, longitudinal inhomogeneity in local critical current in each filament could be characterized. The maximum critical current is 2-3 times higher than the minimum one. It is suggested that the global performance of the wire is limited by some local bottlenecks in each filament.

For quantitative discussion, the value of the local critical current was estimated by considering a model shown in figure 3. The model is illustrated for a *yz* cross-section at a longitudinal position for Filament C. When the filament is magnetized in *z* direction sufficiently, magnetization current flows in $+x$ direction in the left half and in $-x$ direction in the right half. Then, by considering Ampere's law on the small current $(d\theta/2\pi)I_{c,f}$ and its integral along the angle, θ, the following relationship between local magnetic field at the center of the filament, $B_{z,c}$, and local critical current of the filament, $I_{c,f}$, can be obtained analytically:

$$\left|B_{z,c} - B_{ex}\right| = 2\mu_0 \int_0^{\frac{\pi}{2}} \frac{\cos\theta}{2\pi r} \frac{I_{c,f}}{2\pi} d\theta = \frac{\mu_0}{2\pi^2 r} I_{c,f} \quad (1)$$

where μ_0 is the permeability of free space, and r is the radius of the filament. From the equation, the value of local critical current of the filament was evaluated by the measured magnetic field. Critical current of the wire, I_c, was approximately evaluated just by multiplying $I_{c,f}$ by the number of the filaments. Figure 4 shows the results compared with those obtained by four-probe transport method. The value of I_c was estimated using the minimum value of $I_{c,f}$ along the length for each condition. As a result, reasonable agreement with the transport method was observed even with including the temperature dependence. It should be noted that I_c estimated from the SHPM could be directly compared with that from the transport method even if the corresponding electric field criterions were different. This is because electric field dependence of critical current density is very small for MgB_2 especially at lower temperatures and at lower magnetic fields due to very large *n* values. This agreement suggests that the critical currents measured by the four-probe transport method is limited by locally small critical currents in the wire. Therefore, microstructure observation focusing on such positions will be crucial for clarifying performance bottlenecks of the wire.

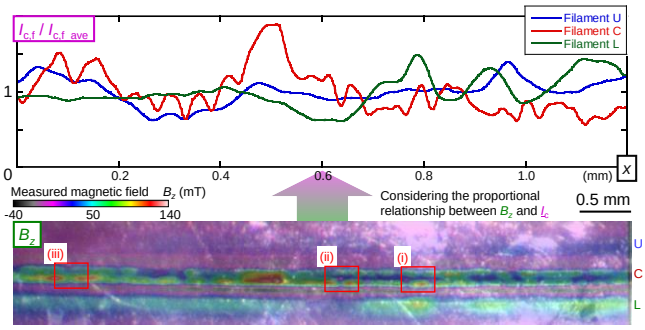

Figure 2. Measured magnetic field distribution in a remanent state at 10 K (lower part) and the corresponding distribution of local critical current for each filament (upper part).

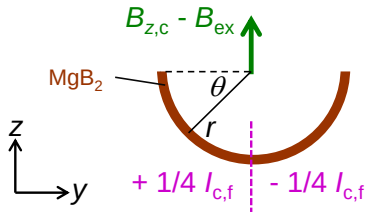

Figure 3. Illustration of a model for the central filament of the wire for estimating the relationship between magnetic field induced by the filament, $B_{z,c}$ - B_{ex}, and critical current of the filament, $I_{c,f}$.

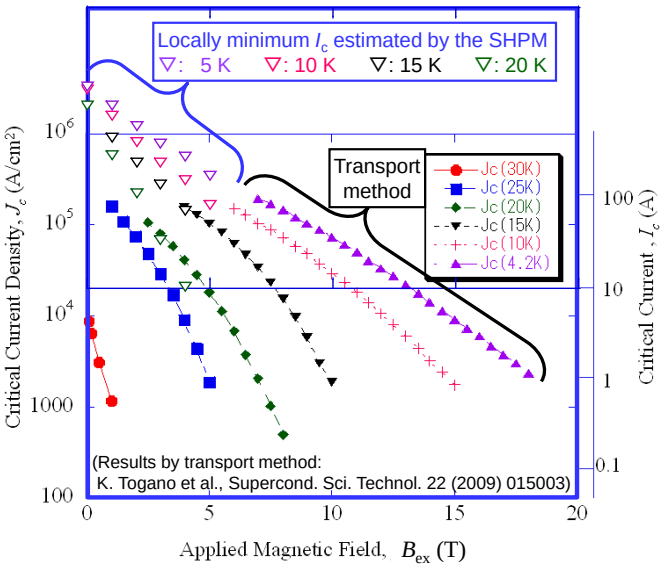

Figure 4. Comparison of critical currents between the estimation by the SHPM and the measurement by the four-probe transport method.

2.3. Site-specific Microstructure Observation

To clarify the origin of locally small critical current, microstructure observation was carried out through SEM. The region (i) shown in figure 2 was selected for the microstructure observation; the region includes locally small critical current around at x = 0.76 mm. Figure 5(a) shows the result compared with the magnetic field distribution taken by the SHPM. Apparently, the magnetic field intensity corresponds well to the volume of the MgB_2 layer. On the other hand, locally small intensity was found even in thick MgB_2 layer as indicated by the broken circle; relatively large deposit was observed at the position in the SEM image. To check the reproducibility of the situation, microstructure observation was carried out also for regions (ii) and (iii) shown in figure 2. Figure 5(b) shows the result for region (ii). Such a deposit, which locally suppressed the magnetic signal, was also observed as shown by the broken circle. Figure 6 shows the situation for region (iii); same situation was confirmed. To clarify the origin of the deposit, elemental mapping was taken for the region. As a result, it was found that the deposit was composed of Mg and Si. This means that the Si originated from SiC addition become an obstacle limiting the performance of the MgB_2 wire. It has been known that MgB_2 wires fabricated with SiC addition include such a deposit, which was analyzed as Mg_2Si [39]. However, for the first time this work gives the direct evidence that Si works as the obstacle of critical current. Furthermore, this study also first clarifies the direct relationship between the performance of the wire and its microstructure based on the hybrid microscopy of the SHPM and SEM. In fact, recent high-performance MgB_2 wires have been fabricated without SiC: C doping by other methods [40-42].

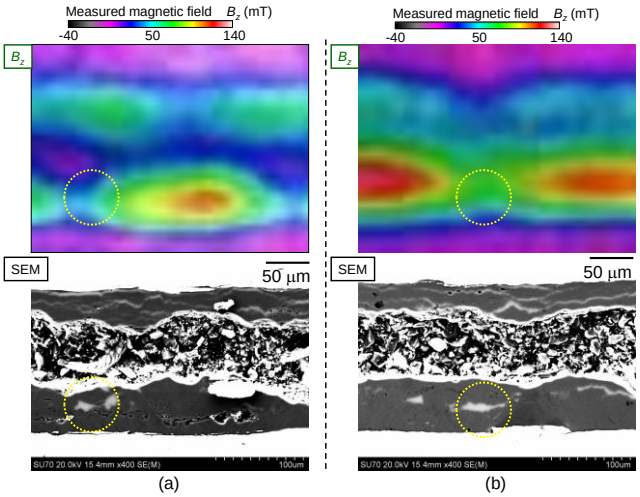

Figure 5. Relationship between magnetic field distribution and SEM image: (a) observation for region (i) in figure 2 and (b) that for region (ii) in figure 2. The broken circle indicates the position of a significant deposit for each figure.

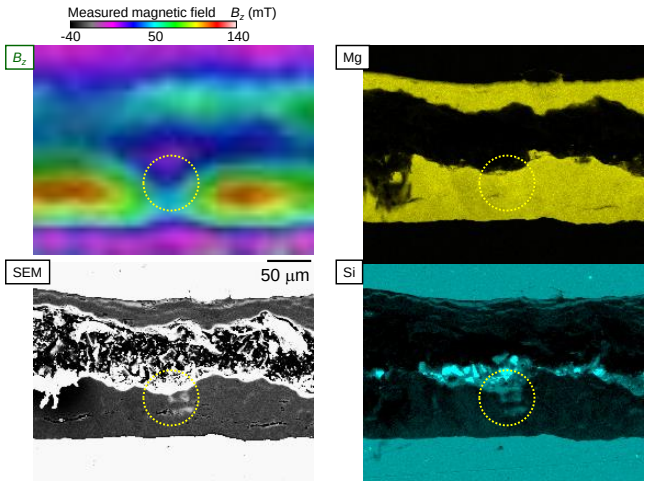

Figure 6. Relationship among magnetic field distribution, SEM image, spatial distribution of Mg, and that of Si for region (iii) in figure 2. The broken circle indicates the position of a significant deposit.

3. Characterization of Long RE-123 Coated Conductor

3.1. Sample and Experimental

The second example is characterization of a commercial RE-123 coated conductor. A 200-m-long 5-mm-wide coated conductor fabricated by IBAD-PLD process was characterized by reel-to-reel scanning Hall-probe microscopy (RTR-SHPM) [43-45]. After continuously magnetizing the sample in a liquid nitrogen bath, two-dimensional distribution of remanent magnetic field was measured by scanning a Hall sensor in width direction on the sample which was moving in longitudinal direction. Step size for the measurement was set to be 33 μm in width direction and 833 μm in longitudinal direction; traveling speed of the sample was set to be 12 m/h; the speed has been being enhanced recently up to 100 m/h which will be presented by another paper. Then the corresponding magnetization current flowing at the amplitude of critical current density was visualized by solving an inverse problem of Biot-Savart law with considering the distance between the active area of the sensor and the superconducting layer in the sample as 250 μm.

3.2. Local Critical Current Distribution in the Sample

Figure 7 shows magnetization current distribution visualized as two-dimensional distribution of sheet current density, J_s; the magnetization current flows to the right in the lower half and to the left in the upper half in the sample. The magnetization current should flow at the amplitude of critical current density according to the critical state model; thus the figure can be seen as in-plane spatial distribution of local critical current density in the sample. Through the whole length, almost homogeneous spatial distribution was confirmed. On the other hand, relatively small intensity was

observed in the lower half periodically as to the longitudinal direction. To check the reproducibility of the situation, another 16-m-long sample was also characterized. Figure 8 shows the result compared with that of TAPESTAR™ [46]. The situation is same also for this sample. Such periodical drops of local critical current were also observed by TAPESTAR™. Although the local I_c drop is not significant as a 5-mm-wide tape, sheet current density drops ~40% in the region (i) compared with the region (ii). This would become a problem in fabricating a narrower tape or a striated multi-filamentary tape. Availability of such information along the width is an advantage of RTR-SHPM compared with TAPESTAR™. Furthermore, this information is indispensable to select precise positions for site-specific characterizations.

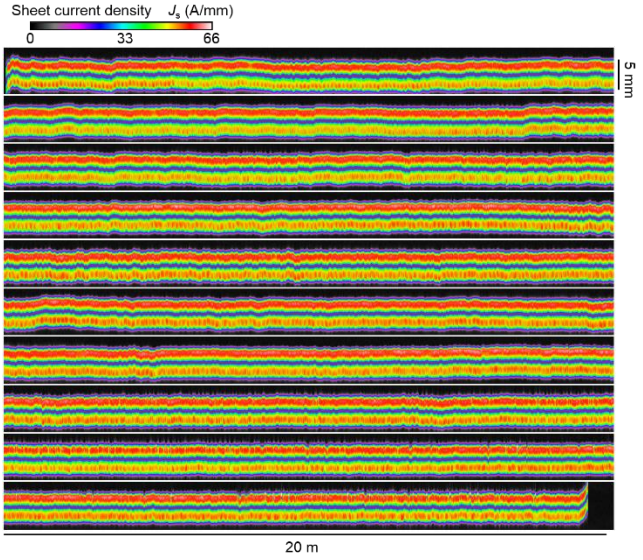

Figure 7. Sheet current density distribution in a 200-m-long 5-mm-wide RE-123 coated conductor characterized by RTR-SHPM.

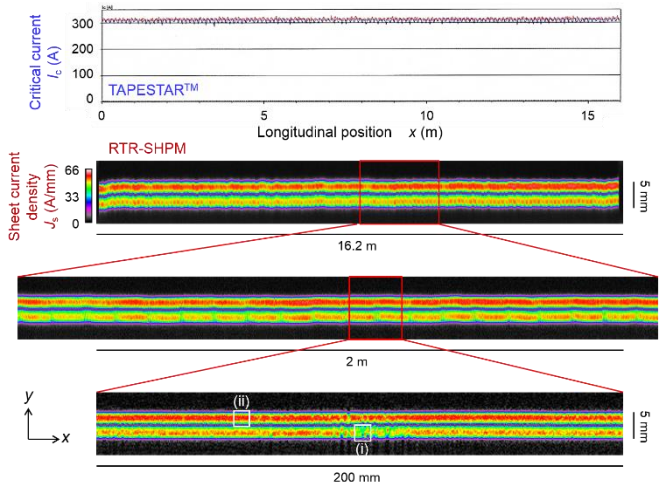

Figure 8. Sheet current density distribution in a 16-m-long 5-mm-wide RE-123 coated conductor characterized by RTR-SHPM compared with critical current distribution characterized by TAPESTAR™.

3.3. Discussion on the Local Critical Current Distribution

To discuss the validity and the origin of the results, additional measurements were carried out for regions (i) and (ii) indicated in figure 8. Figure 9 shows the results. X-ray micro tomography (Bruker Skyscan 1172) was applied with spatial resolution of 2 μm/pixel to check the difference in microstructure between the regions. Then local critical current for each region was measured by four-probe method with a 0.5-mm-long 0.1-mm-wide micro-bridge. Good correspondence of local critical currents between RTR-SHPM and four-probe method was confirmed: ~40% lower value in region (i) than in region (ii). The difference of the values between the methods originated from that of electric field criterion: ~10^{-8} V/m for RTR-SHPM and 10^{-4} V/m for four-probe method. As seen in the difference in local critical current, clear difference in microstructure was also observed. The images were picked up as plan views at depth positions on the superconducting layer and on the Hastelloy substrate. Similar structures were observed for both depth positions. It is suggested that the smaller local critical current in region (i) is originated from the defects induced from those on Hastelloy substrate. Thus, it could be concluded that pretreatment of the surface of Hastelloy substrate is still important. In this way, the direct relationship between the performance of the 200-m-long coated conductor and its local microstructure was confirmed, and the origin of the performance bottleneck was clarified successfully.

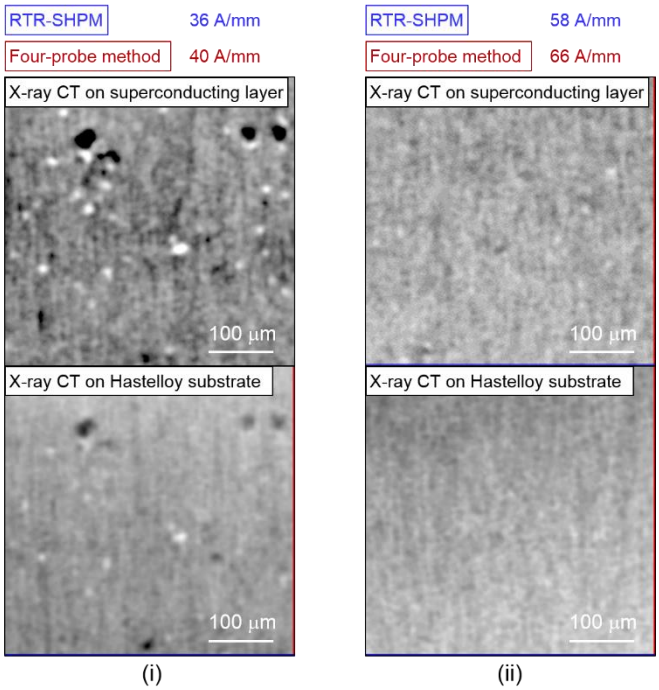

Figure 9. Images picked up as *xy* cross-sections (parallel to the tape surface) at depth positions near the top surfaces of the superconducting layer and the Hastelloy substrate. The corresponding values of critical current per width are also listed. The positions of the regions (i) and (ii) are indicated in figure 8.

4. Characterization of Striated Multi-filamentary Coated Conductor

4.1. Sample and Experimental

The third example is characterization of a striated multi-filamentary coated conductor. The sample was fabricated by laser scribing method with the combination with wet etching [47, 48]; five filaments were patterned on a 5-mm-wide coated conductor. The magnetization current flowing at the amplitude of critical current density was characterized by an SHPM system [49-51].

4.2. Local Critical Current Distribution in the Sample

Figure 10 shows the result obtained in a remanent state at 79 K. The measurement was carried out with step size of 20 μm in width direction and 200 μm in longitudinal direction; it took 120 minutes to take the image. Magnetization current flowing in each filament was successfully visualized by considering the distance between the active area of the sensor and the superconducting layer in the sample as 260 μm; the intensity can be seen as that of local critical current according to the critical state model. The filaments are separated well each other. On the other hand, some defects were observed in the lowermost filament. To see the detail, figure 11 shows an enlarged image for the region indicated by the solid rectangular in figure 10. To check the origin of the situation, the regions (i)-(iv) were selected for microstructure observation.

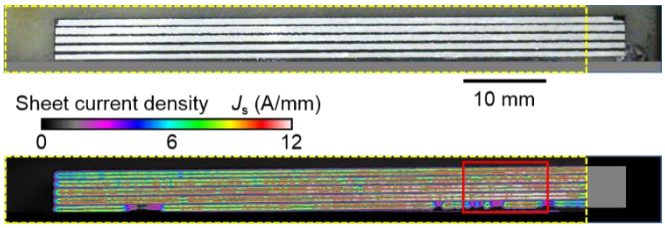

Figure 10. Photograph of the sample of 5-mm-wide 5-filamentary coated conductor and its sheet current density distribution obtained by SHPM in a remanent state at 79 K. The broken rectangular indicates the measurement region of SHPM. The solid rectangular indicates the focused region shown in figure 11.

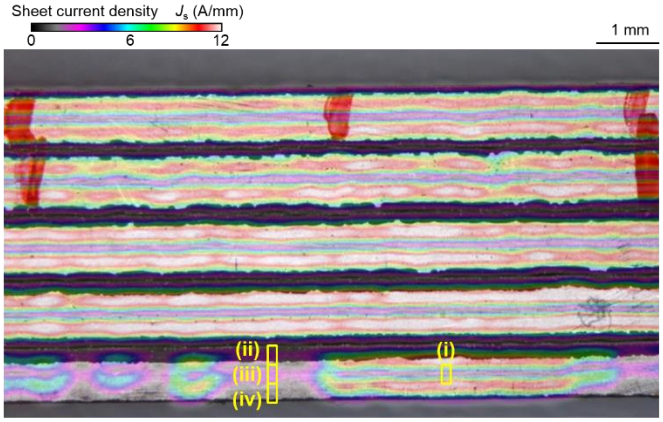

Figure 11. Enlarged figure for the region indicated in figure 10 and selected positions for SEM observation.

4.3. Site-specific Microstructure Observation

The region (i) was selected as a reference for good property. Figure 12 shows images taken for its cross-section through SEM. By elemental mapping, positions of the components were identified: Hastelloy, GdBCO superconducting layer, Ag, etc. No significant defects were observed for this region as expected. On the other hand, figure 13 shows images taken for regions (ii)-(iv). Significant defects were observed for regions (iii) and (iv): voids spread inside the superconducting layer. Considering the situation that region (ii) did not include such a significant defect, this would not be related from the scribing process but from the original edge of the sample. To discuss the reason of the defect, detailed image was taken for region (iii) through TEM. Even in the superconducting layer above the void (indicated by “a”), GdBCO remains. This means that such void was introduced after the deposition of the GdBCO superconducting layer. It is also suggested that etchant used in the wet etching process infiltrated into the voids to dissolve the GdBCO to polycrystalline materials (indicated by “b” and “c”). From these findings, it could be concluded as follows. First, the laser scribing method would not have a significant problem. Second, treatment for the original edge of the tape is important. Third, it would be preferable to omit the wet etching process if possible. In fact, taking care of these findings, the striation process have been modified and improved recently [52].

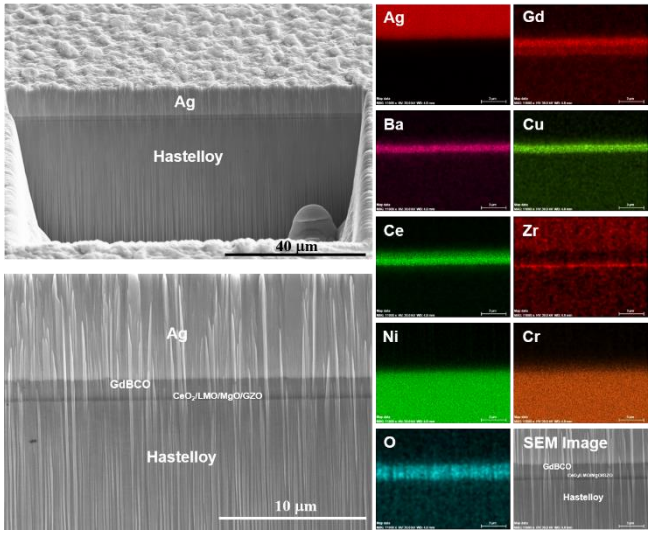

Figure 12. Images taken by SEM for a cross-section of region (i) indicated in figure 11.

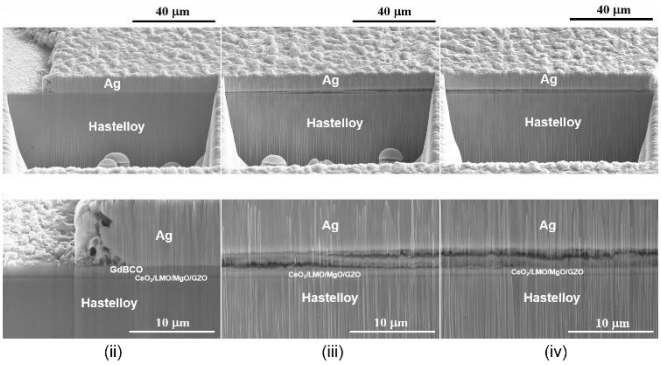

Figure 13. Images taken by SEM for a cross-sections of regions (ii)-(iv) indicated in figure 11.

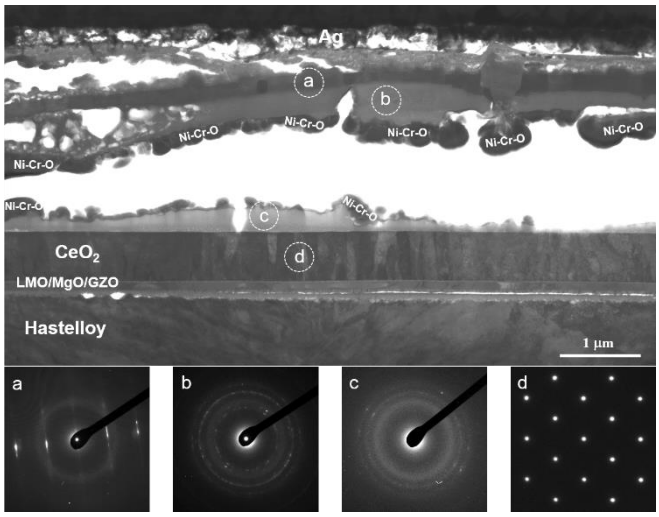

Figure 14. Images taken by TEM for a cross-section of region (iii) indicated in figure 11.

5. Conclusion

Characterization results of superconducting wires and tapes based on scanning Hall-probe microscopy were reported in this paper. This technique offered information on local critical current (density) distribution in them with spatial resolution of submillimeters to several tens of micrometers from the practical-scale samples. This information worked very well for selecting positions for microstructure observations such as SEM, TEM, and X-ray CT. As a result, direct relationships between their performances and the corresponding micro-scale or nano-scale structures were clarified. From these findings, processes in fabricating them have been modified and improved successfully in these years. We believe that this diagnostic scheme will work better for further developments of superconducting wires and tapes.

Acknowledgements

This work was supported by the JSPS KAKENHI (Grant Number JP19H05617 and JP18K18864), the Japan Science and Technology Agency (JST) through the Advanced Low Carbon Technology Research and Development Program (ALCA), and by the New Energy and Industrial Technology Development Organization (NEDO).

References

[1] Selvamanickam V et al. 2007 *IEEE Trans. Appl. Supercond.* **17** 3231
[2] Kutami H et al. 2009 *Physica C* **469** 1290
[3] Lee J-H et al. 2014 *Supercond. Sci. Technol.* **27** 044018
[4] Lee S et al. 2014 *Supercond. Sci. Technol.* **27** 044022
[5] Prusseit W et al. 2006 *Journal of Physics: Conference Series* **43** 215
[6] Liu L et al. 2015 *IEEE Trans. Appl. Supercond.* **25** 6604804
[7] Zhang W et al. 2007 *Physica C* **463-465** 505
[8] Hahn S et al., 2019 *Nature* **570** 469
[9] Maeda H et al. 2019 *IEEE Trans. Appl. Supercond.* **29** 4602409
[10] Oya M et al. 2018 *IEEE Trans. Appl. Supercond.* **28** 4401205
[11] Miyazaki H et al. 2016 *Supercond. Sci. Technol.* **29** 104001
[12] Winkler T et al. 2019 *IOP Conf. Series: Materials Science and Engineering* **502** 012004
[13] Komiya M et al. 2019 *IEEE Trans. Appl. Supercond.* **29** 5204306
[14] Ayai N et al. 2008 *Physica C* **468** 1747
[15] Yumura H et al. 2009 *IEEE Trans. Appl. Supercond.* **19** 1698
[16] Yumura H et al. 2013 *IEEE Trans. Appl. Supercond.* **23** 5402306
[17] Hanai S et al. 2017 *IEEE Trans. Appl. Supercond.* **27** 4602406
[18] Hashi K et al. 2015 *Journal of Magnetic Resonance* **256** 30
[19] Terao Y et al. 2013 *IEEE Trans. Appl. Supercond.* **23** 4400904
[20] Tomsic M et al. 2007 *Physica C* **456** 203
[21] Stenvall A et al. 2006 *Supercond. Sci. Technol.* **19** 184
[22] Tanaka K et al. 2005 *Supercond. Sci. Technol.* **18** 678
[23] Vysotsky V et al. 2015 *IEEE Trans. Appl. Supercond.* **25** 5400205

[24] Atomura N et al. 2012 *Physics Procedia* **27** 400
[25] Kajikawa K et al. 2009 *IEEE Trans. Appl. Supercond.* **19** 1669
[26] Tarantini C et al. 2011 *Physical Review B* **84** 184522
[27] Zhang X et al. 2017 *IEEE Trans. Appl. Supercond.* **27** 7300705
[28] Nishijima G et al. 2008 *IEEE Trans. Appl. Supercond.* **18** 1131
[29] Matsumoto S et al. 2012 *IEEE Trans. Appl. Supercond.* **22** 9501604
[30] Awaji S et al. 2010 *IEEE Trans. Appl. Supercond.* **20** 592
[31] Ma D X et al. 2014 *Supercond. Sci. Technol.* **27** 085014
[32] Cobb C B et al. 2002 *Physica C* **382** 52
[33] Lu J et al. 2011 *IEEE Trans. Appl. Supercond.* **21** 3009
[34] Goldacker W et al. 2006 *Journal of Physics: Conference Series* **43** 901
[35] Weiss J D et al. 2017 *Supercond. Sci. Technol.* **30** 014002
[36] Togano K et al. 2009 *Supercond. Sci. Technol.* **22** 015003
[37] Higashikawa K et al. 2014 *Physica C* **504** 62
[38] Higashikawa K et al. 2016 *IEEE Trans. Appl. Supercond.* **26** 6200804
[39] Shimada Y et al. 2011 *Physica C* **471** 1137
[40] Li G Z et al. 2013 *Supercond. Sci. Technol.* **26** 095007
[41] Ye S J et al. 2014 *Supercond. Sci. Technol.* **27** 085012
[42] Xu D et al. 2016 *Supercond. Sci. Technol.* **29** 045009
[43] Higashikawa K et al. 2014 *IEEE Trans. Appl. Supercond.* **24** 6600704
[44] Higashikawa K et al. 2017 *IEEE Trans. Appl. Supercond.* **27** 6603004
[45] Higashikawa K et al. 2017 *IEEE Trans. Appl. Supercond.* **27** 8001404
[46] Furtner R et al. 2004 *Supercond. Sci. Technol.* **17** S281
[47] Suzuki K et al. 2007 *Supercond. Sci. Technol.* **20** 822
[48] Machi T et al. 2013 *Supercond. Sci. Technol.* **26** 105016
[49] Higashikawa K et al. 2011 *Physica C* **471** 1036
[50] Higashikawa K et al. 2012 *IEEE Trans. Appl. Supercond.* **22** 500704
[51] Higashikawa K et al. 2013 *IEEE Trans. Appl. Supercond.* **23** 6602704
[52] Machi T et al. 2018 *Journal of Physics: Conference Series* **1054** 012033